Journal of Nuclear Materials 408 (2011) 289–295

Contents lists available at ScienceDirect

Journal of Nuclear Materials

journal homepage: www.elsevier.com/locate/jnucmat

Three-dimensional characterization of stress corrosion cracks

S. Lozano-Perez [a,*], P. Rodrigo [b], Lionel C. Gontard [c]

[a] University of Oxford, Department of Materials, Parks Road, Oxford OX1 3PH, UK
[b] Universidad Rey Juan Carlos, Dpto. de Ciencia e Ingeniería de Materiales, c/ Tulipán s.n., 28933 Móstoles (Madrid), Spain
[c] Danish Technical University, Center for Electron Nanoscopy, Matematiktorvet Building 307, Room 115, 2800 Kogens Lyngby, Denmark

ARTICLE INFO

Article history:
Received 29 April 2010
Accepted 28 November 2010
Available online 4 December 2010

ABSTRACT

Understanding crack propagation and initiation is fundamental if stress corrosion cracking (SCC) mechanisms are to be understood. However, cracking is a three-dimensional (3D) phenomenon and most characterization techniques are restricted to two-dimensional (2D) observations. In order to overcome this problem, different approaches to extract 3D information have been used in the recent years. In this work we will present the benefits of using 3D focused ion beam (FIB) slicing and electron tomography. 3D FIB slicing offers a fast and high throughput characterization while electron tomography offers the best spatial resolution. To illustrate the power of these techniques, different parts of dominant stress corrosion cracks in Ni-alloys and stainless steels have been reconstructed in 3D. All relevant microstructural features can now be studied in detail and its relative orientation respect to the strain direction and grain boundary plane accurately measured.

1. Introduction

Low potential stress corrosion cracking (LPSCC) of Ni-alloys and stainless steels is a very important degradation phenomenon in pressurized water reactors (PWRs). Although SCC of austenitic steels has not been reported yet in operating PWR plants (except from irradiated materials), careful autoclave testing in under controlled environments have confirmed that highly cold worked stainless steels are susceptible to SCC even in PWR primary water conditions [1]. Ni-alloys, on the other hand, are well known for suffering from SCC under PWR conditions [2].

Conventional characterization techniques used to study crack initiation and propagation have been typically restricted to two-dimensional observations, providing incomplete information on the cracking phenomena. In order to overcome this problem, different approaches to extract 3D information have been used. Amongst these are 3D focused ion beam (FIB) slicing [3], acoustic microscopy and X-ray tomography [4–7]. In this work, 3D FIB slicing has been applied to the characterization of several stress corrosion cracks from different PWRs materials, offering a good compromise between spatial resolution and amount of volume examined. The technique has proven very useful to reveal the interaction between the crack and the different microstructural defects. It has also been used to reconstruct the volume occupied by the oxide filling the open crack. However, this method still has limited resolution and does not provide detailed information from the crack tip region nor its chemistry.

Electron tomography offers better spatial resolution but can only provide information from much smaller volumes. However, it can also provide accurate crystallographic and chemical information. Both in TEM and STEM mode, it has been extensively applied to the characterization of complex systems which include studies of nanocomposites of FeAl + Y_2O_3, carbon nanotubes, Si particles embedded in SiO_x, Pt catalysts nanoparticles, scanning tunnelling microscopy probes, polyhedral particles of CeO_2, polymers, dislocations and magnetic rings [8–15], amongst others. In this paper, we use electron tomography to characterize crack tips in cold worked steels with complex microstructure.

2. Materials and methods

The materials employed in this study were Japanese grade 304 stainless steel (SUS304). Its composition was, in weight%, 0.04 C, 0.31 Si, 1.59 Mn, 0.031 P, 0.001 S, 0.24 Cu, 9.21 Ni, 0.34 Mo, 18.34 Cr and balance of Fe. The alloy was solution treated at 1060 °C for 100 min and then water-quenched. The specimens were unidirectionally cold-rolled to a reduction of 5%, 10% and 20% in thickness (5%, 10% and 20% cold work or CW). SCC tests were performed under constant load (30 MPa $m^{1/2}$) in a simulated PWR primary water chemistry (500 ppm B + 2 ppm Li, + 30 cc-STP/kg-H_2O DH_2) at 320 °C.

FIB 3D slicing was performed in a Zeiss NVision 40 dual-beam FIB operated at 30 keV for Ga^+ ions and 2 keV for electrons. Optimum imaging conditions were selected before starting the automated slicing sequence and a secondary electron (SE) detector used. Image distortions due to sample tilt were corrected during the acquisition by the microscope software. Trenches were milled

* Corresponding author. Tel.: +44 (0)1865 273707.
E-mail address: sergio.lozano-perez@materials.ox.ac.uk (S. Lozano-Perez).

0022-3115/$ - see front matter © 2010 Elsevier B.V. All rights reserved.
doi:10.1016/j.jnucmat.2010.11.068

around volume of interest to avoid re-deposited material obstructing the area of interest. A milling current of 700 pA was found a good compromise between milling time and surface quality. Spacing between slices was fixed to ~40 nm. Series acquisition typically required several hours. Image cross-correlation was performed using markers outside the sampled volume and the region of interest on the cross-sectional view was extracted automatically. Drift between consecutive slices (in the milling direction) was measured to be smaller than 5 nm and has not been taken into account in the reconstruction. The final datacube containing the 3D information was segmented and reconstructed for 3D visualization using Mercury Software's Avizo.

The TEM samples used for the electron tomography experiments were prepared to contain dominant cracks using the in situ lift out technique [16] in a FEI 200 single beam FIB. As can be seen in Fig. 1a, polishing a cross-section with a sub-micron silica suspension revealed the location of the cracks and the region chosen for the TEM sample preparation is shown boxed (Sample SUS304 5%CW). After extracting the volume containing the crack tip, it was welded to the tip of a dedicated Fischione tomography Cu post (designed for its 360° on-axis rotation holder model 2050) as shown in Fig. 1b. Once secured at the tip of the Cu post, it was thinned to electron transparency and, as shown in Fig. 1c, the location of the crack tip was successfully preserved inside the extracted volume. This TEM sample contained three different grains, labelled G1, G2 and G3 and three grain boundaries, gb1, gb2 and gb3. Tomographic tilt series up to ±80°, every 1° or 2° were acquired using a probe-corrected FEI Titan field-emission gun (FEG) TEM operated in STEM mode at 300 kV and a Jeol 3000F operated at STEM mode at 297 kV. The 3D shapes were obtained using high-angle annular dark field (HAADF) STEM tomography [17] using a collection aperture semi-angle >70 mrad. HAADF images from the selected crack tips are shown in Fig. 2. As can be seen, not all the diffraction contrast has disappeared, which was useful to observe the location and orientation of the grain boundaries and twin deformation bands (TDBs). The oxides can be clearly distinguished due to their lower atomic number (and therefore, lower intensity in the HAADF image). Alignment and reconstruction of the datasets was performed using the simultaneous iterative reconstruction technique (SIRT) algorithm [18] in Inspect3D (FEI) software (15–20 iterations proved to be enough to reach convergence). Visualization of the final 3D datasets was performed by surface segmentation in Amira V2.3 (Indeed – Visual Concepts GmbH) and Avizo 5.1 (Mercury Software) associating different intensities in the image to different material densities.

Chemical analysis was performed in the Jeol 3000F, operated at 297 kV and equipped with a Gatan Image Filter (GIF™) 2000. EELS spectrum images were acquired drift corrected using a convergence half-angle of 12 mrad and a collection half-angle of 9 mrad. The dwell time per pixel was 0.2 s and drift correction was performed automatically every 10 s. Spectrum images were processed using multivariate statistical analysis as described in [19]. Typical EELS spectra from the matrix, Cr-rich and Fe-rich spinel oxides are shown in Fig. 3.

3. Results

3.1. FIB 3D slicing

FIB 3D slicing has been used to characterize different aspects of crack initiation and propagation in austenitic stainless steels and nickel alloys tested under simulated PWR primary water conditions. Tensile test samples containing shallow cracks (Inconel 600) and ½ CT specimens with long deep cracks (SUS304) were used to extract 3D information about the crack tip and oxide morphology.

TDBs caused by cold work in 404SS are known to suffer from preferential oxidation [20]. As the crack advances, those TDBs intersecting the crack flanks become exposed to the environment and oxidize. A region containing a portion of the crack and a grain with some visible TDBs was selected for analysis. In Fig. 4a, a SEM SE image from a cross-sectional view reveals the location of the main crack (left, diagonal) and a secondary one (right, vertical).

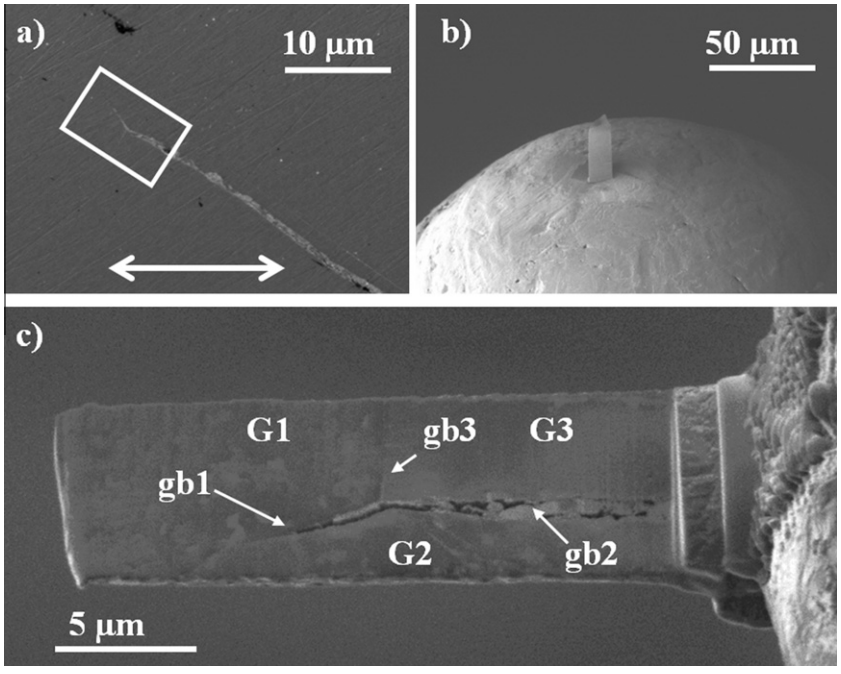

Fig. 1. FIB SE images showing: (a) cross-sectional view with SCC crack chosen for tomography boxed (arrow indicates strain direction during SCC test), (b) plan-view specimen containing the crack tip after welding to the tomography post and (c) plan-view TEM sample welded to tomography post before final thinning. The location of all grains and grain boundaries has been indicated. Sample: SUS304 5%CW.

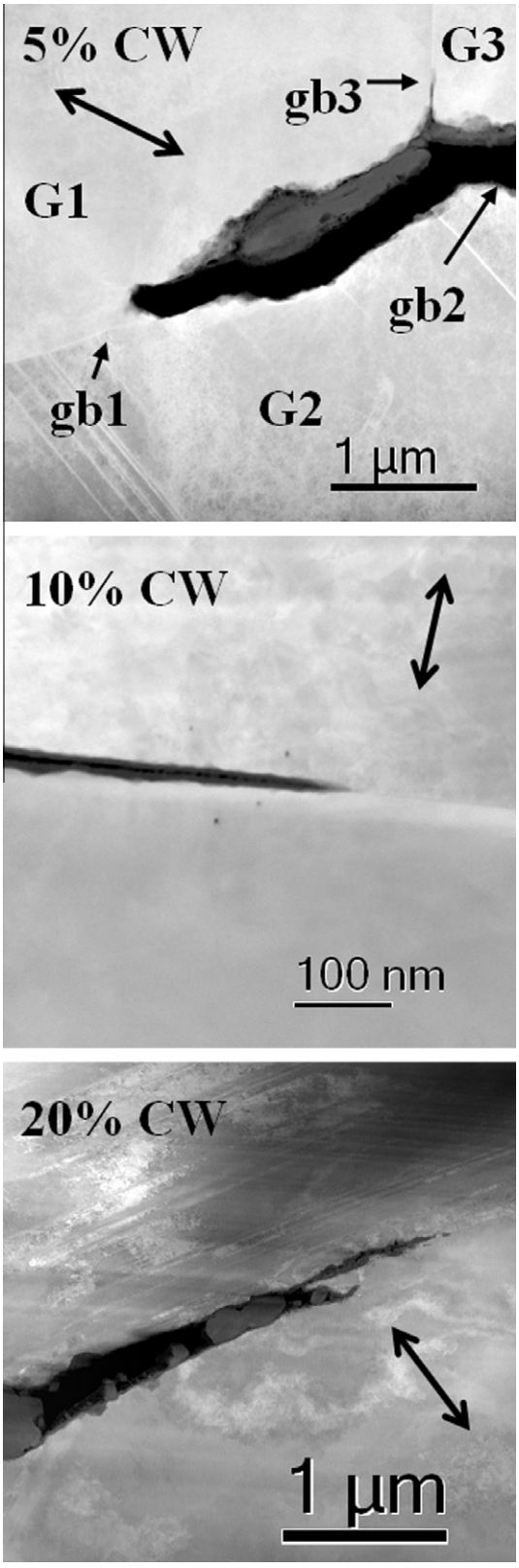

Fig. 2. STEM ADF image showing the crack tips chosen for the tomographic reconstruction. The high dislocation density and the location of several TDBs are clearly visible. Grains are labelled as G1, G2 and G3. Grain boundaries are labelled as gb1, gb2 and gb3. Double-headed arrow indicates strain direction. Samples: SUS304 with different levels of cold work.

The grain on top of the main crack has several oxidized TDBs. A volume of 20 × 6 × 5 μm was milled away after 125 slices and reconstructed in 3D, as it shown in Fig. 4b. Oxidized regions are clearly visible in SEM SE images as they are characterized by lower SE count production than the matrix, therefore appearing darker in the images. This is caused by their lower average atomic number and density and was further confirmed by microanalysis in the TEM.

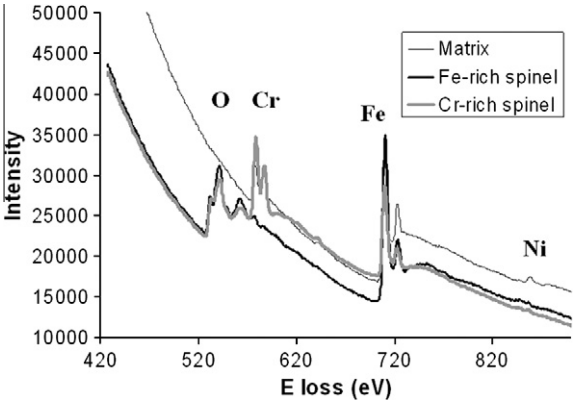

Fig. 3. Representative EELS spectra extracted from the matrix region, Fe-rich spinel oxide and Cr-rich spinel oxide. Sample: SUS304 with 20%CW.

Inconel 600 exposed to PWR primary water suffers from severe grain boundary oxidation [21]. A shallow crack from an Inconel 600 tensile test specimen was selected for 3D reconstruction in an attempt to observe how the presence of the crack affected the oxidation of the adjacent grain boundaries. Several grain boundaries were found oxidized in the selected volume and have been included in the 3D visualization. In Fig. 5a, one of the first slices (SEM SE image) is shown together with the reconstructed volume. It can be seen that the crack had not reached the first triple point when the autoclave test concluded. The dark contrast at the grain boundaries ahead revealed the presence of oxide. The original sample surface (exposed to the environment) corresponds to the top face of the box. The crack (dark colour) and the oxidized portion of the grain boundaries (light colour) ahead of the triple point have been segmented (see Fig. 5b) and rendered in 3D.

3.2. Electron tomography

A dominant crack tip was extracted from several ½ CT SUS304 specimens tested under constant load in simulated PWR primary water. Specimens had previously been cold-rolled to a reduction in thickness of 5%, 10% and 20%. Cold worked samples exhibit a complex microstructure with high density of TDBs and dislocations [20]. All TEM samples examined showed a much higher density of TDBs in one of the grains. The 20%CW sample had a TDB density of ~34/μm, while the 10%CW had ~30/μm and the 5%CW ~3/μm in the analyzed grains. Apart from the abrupt drop in TDB density between the 10% and the 5%CW samples, it should also be noted that while in the 20% and 10% samples the distribution was homogeneous along the grain, in the 5%CW sample it was heterogeneous, with regions up to 1 μm along the grain boundary without any observable TDB (see Fig. 2). The 20%CW sample had a bifurcated crack tip, with one of the cracks growing transgranularly. The intergranular portion had developed an oxide on the flanks ~30 nm wide and open portions ~10 nm wide. The 10%CW sample exhibited an intergranular crack which had developed an oxide on the flanks ~5 nm wide and open portions ~5 nm wide near the tip. The 5%CW sample, unlike the others, exhibited a blunted crack tip, which did not show signs of oxidation on the flanks near the tip and had an open portion of ~200 nm.

The reconstructed volumes from the regions shown in Fig. 2 can be seen in Fig. 6. The volume shown from the SUS304 5%CW

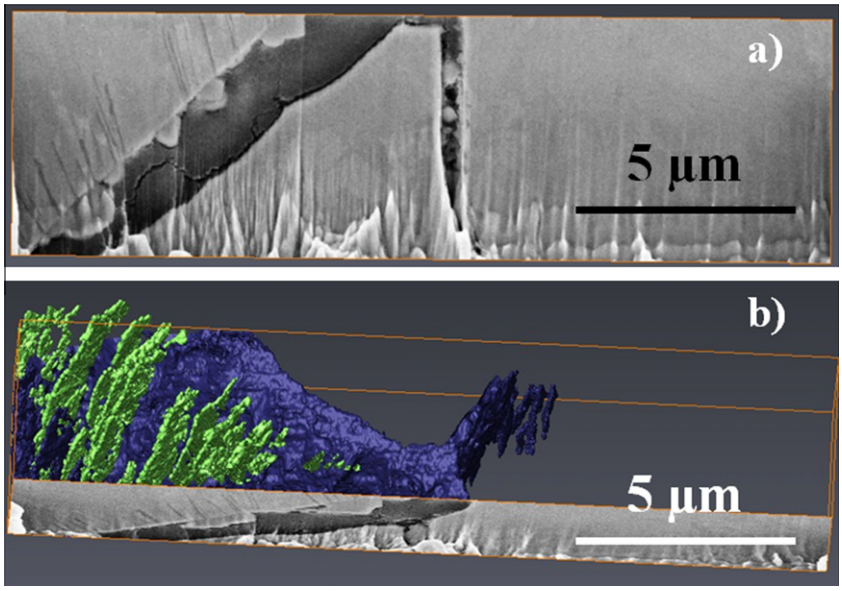

Fig. 4. (a) SEM SE image showing an image from a FIB 3D slicing series. Two cracks are visible, with the diagonal one showing signs of TDB oxidation on the top grain (darker contrast) and (b) reconstructed volume showing the volume of the open crack (dark) and the oxidized TDBs (light), together with one of the original slices. Sample: SUS304 20%CW.

dataset contains microstructural features such as grain boundary planes (gb1, gb2 and gb3) and TDB planes, as well as the oxides products (Fe-rich + Cr-rich spinel). The volumes from the 10% and 20%CW samples only show the two oxide phases.

As can be seen in Fig. 7, the samples used for electron tomography can also be characterized using any of the analytical techniques available in the (S)TEM. In this case, EELS spectrum imaging (SI) was used to analyze the oxidation at the crack tip from the boxed region shown in Fig. 6c. As previously observed [20], the flanks of the crack have oxidized and Cr-rich spinel has been formed. The formation of Cr-rich spinel displaces the Ni (which does not oxidize in the hydrogenated water used for the test) along the grain boundary, forming a Ni-rich region at the interface between the Cr-rich oxide and the metal. The open portions of the boundary, where cracking has occurred, were found filled by Fe-rich spinel.

Other regions of interest from the SUS304 5%CW, including the crack flanks at ~3 μm from the tip (Fig. 8) and an oxidized cell inside a TDB near the crack flank (Fig. 9), were also reconstructed.

We have made use of the preserved elastic contrast in the SUS304 5%CW dataset, in order to reconstruct the location of three grain boundary planes (gb1, gb2 and gb3) and several TDBs, as can be seen in Figs. 6a and 9b. The relative orientation of these features respect to the strain direction or TEM foil plane was measured and it is listed below:

- Original ½ CT specimen orientation respect to the CW rolling direction was T–S. This can also be taken as the orientation of the TEM sample, as it was extracted in plan-view.
- The strain direction during the constant load test is contained in the plane of the TEM sample and indicated by the double-headed arrow in Fig. 2a. It was measured to be at 60 ± 1° from the intergranular crack growth direction (gb1).
- The plane containing gb1, containing the crack tip, was measured to be at 8 ± 1° from the plane containing the TEM sample.
- The family of TDBs visible in grain 2 (G2) in Fig. 2a are all parallel to each other and form an angle of 71 ± 1° with the gb1 plane and an angle of 7 ± 1° with the plane of the TEM sample.
- The same family of TDB was characterized in the region on the right of the area shown in Fig. 2a (shown in Fig. 9). In that area, the crack advanced along a different grain boundary (gb2) containing the same grain (G2). Gb2 was forming an angle of 16 ± 1° with the TEM sample plane and 25 ± 1° with the strain direction. The TDBs formed an angle of 44 ± 1° with gb2.
- A portion of a TDB in G2 was found to be oxidized (see Fig. 9). The oxide, identified as Cr-rich spinel, was fully enclosed in the TDB plane but growing at an angle of 28 ± 1° respect the TEM foil plane (see Fig. 9c).

4. Discussion

Since cracking and oxidation of stainless steels and Ni-alloys in PWRs occur in a three-dimensional way, it seems logical to attempt a 3D characterization. As described in the previous sections, FIB 3D slicing and electron tomography have been used to reconstruct selected regions along the crack path. Although capable of providing more information than conventional 2D approaches, these techniques require special visualization methods and a more complex interpretation.

The 3D FIB slicing technique is a relatively fast way of obtaining information on the crack tip morphology, cracking mode (intergranular, transgranular), location of oxide products, inclusions and microstructural features (if channelling contrast is available). New generation dual-beam FIBs allow for the full automation of the process, requiring little interaction from the operator. Image resolution is limited in the *x*-sectional surface by the achievable electron probe size (typically ~1 nm) and/or the number of pixels used for the image acquisition. In the transversal (or milling) direction, spatial resolution in the reconstruction is limited by the stage and Ga^+ optics stability during the slicing sequence. Image registration and datacube generation can be done by many image processing packages with sub-pixel accuracy [22]. In this work, Gatan's Digital Micrograph™ was used for that purpose. Segmentation of the features of interest was performed automatically for easily differentiated features such as oxide particles or empty cracks (where simple thresholding of the intensity was sufficient), or manually for more subtle features such as oxidized grain boundaries or TDBs. In Fig. 4a, the location of the oxidized TDBs is clear on the SE image (due to its lower signal intensity), and was used to generate the 3D representation in Fig. 4b. Electron back scattering diffraction

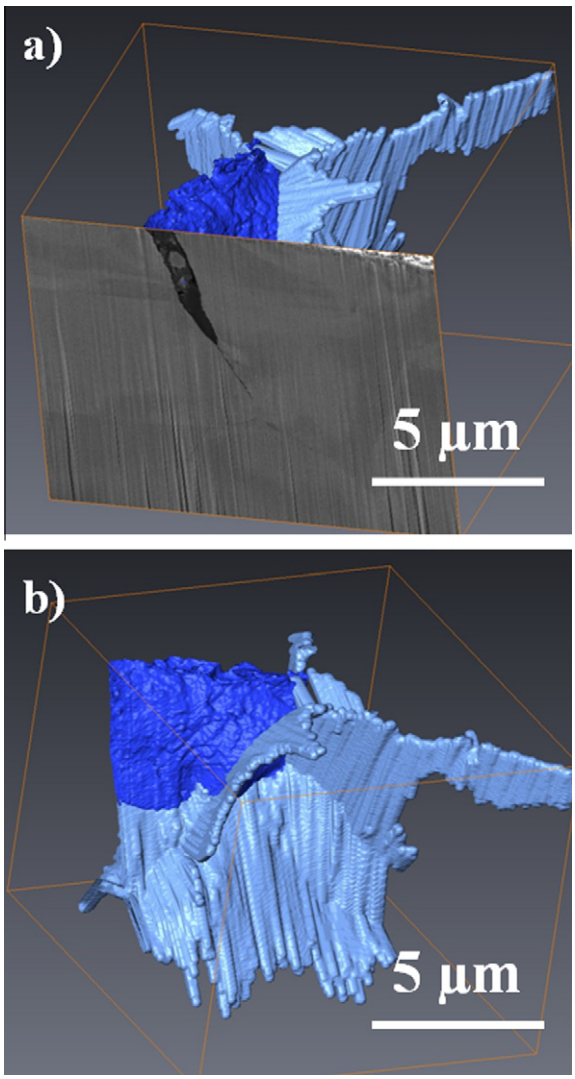

Fig. 5. (a) SEM SE image from the 3D slicing series together with the reconstructed model and (b) reconstructed model showing the open crack (dark) and the oxidized grain boundaries (light). Sample: Alloy 600.

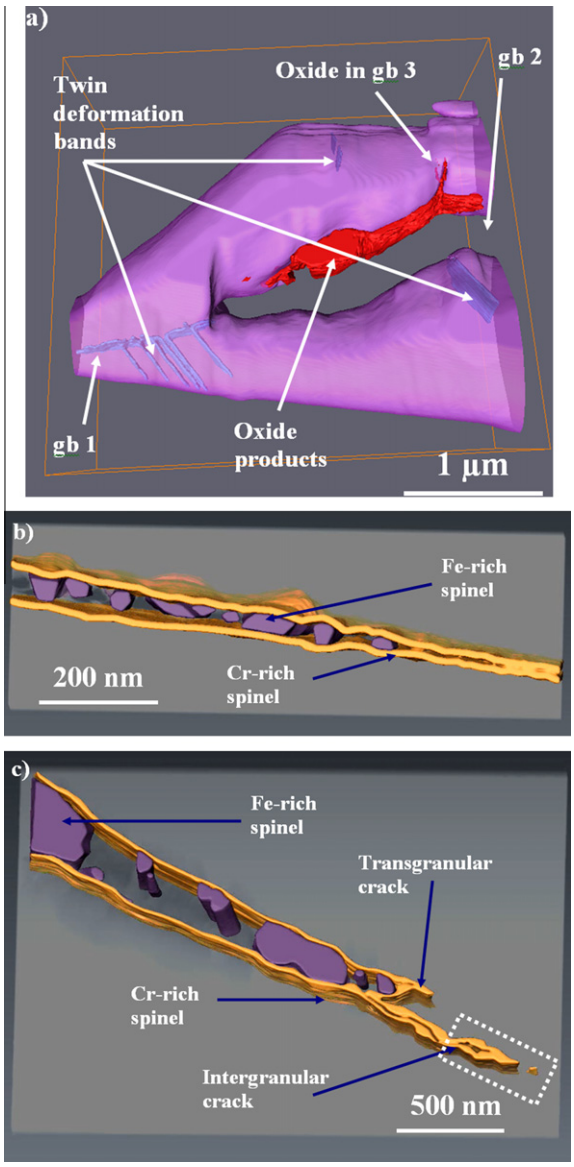

Fig. 6. 3D models representing the crack tip volume: (a) sample: SUS304 with 5%CW, (b) SUS304 with 10%CW and (c) SUS304 with 20%CW.

(EBSD) and TEM analysis (not shown in this paper) revealed that TDBs appear along {1 1 1} planes. The characterization of up to 15 TDB's oxidized portions revealed that, on that particular grain, they oxidized to an average depth of 1.5 ± 0.2 μm from the crack flank and lengths beyond 5 μm along the flank, always parallel to the same (1 1 1) plane.

The analysis of the reconstruction of the shallow crack in the Inconel 600 sample (Fig. 5) indicates that although the crack grew intergranularly to an average depth of 4 μm, a network of oxidized grain boundaries extended much further to depths of more than 10 μm. Every grain boundary intersecting the surface exposed to the environment in the reconstructed volume was found to be oxidized. The extent of the oxidation was found to decrease moving away from the open crack.

Electron tomography has been applied for the first time to the analysis of stress corrosion crack tips, providing 3D reconstructions of three crack tips extracted from SUS304 samples with different levels of cold work. When trying to understand the mechanisms governing crack propagation in cold work stainless steels, it is important to know how the microstructure interacts with the crack as it advances. In particular, in order to model stresses at the tip region, the relative orientation of features like grain boundary planes or TDBs respect to the strain direction are required. For this reason, being able to identify the contrast from the microstructural defects through most of the tilt series is very important and will be discussed next.

Many of the images in the tilt series of HAADF images show abrupt changes in contrast at boundaries between adjacent grains (see Fig. 2). In our experiment such variations in contrast cannot be associated with compositional segregation but from diffraction effects related to crystal orientation or from strain resulting from imperfection of the crystal structures at the boundaries. HAADF contrast usually depends on a combination of specimen thickness, composition, specimen orientation and detector inner angle. The presence of thermal diffuse scattering (TDS) and multiple scattering make the quantitative interpretation of the contrast difficult. Resonant phonon modes can occur close to twin boundaries and enhance TDS [23], and localized static strain can give rise to HAADF contrast similar to that arising from variations in composition or thickness [24] showed that ADF images of B-doped silicon can exhibit opposite contrast to that expected as a result of scattering from displaced atoms surrounding impurity atoms.

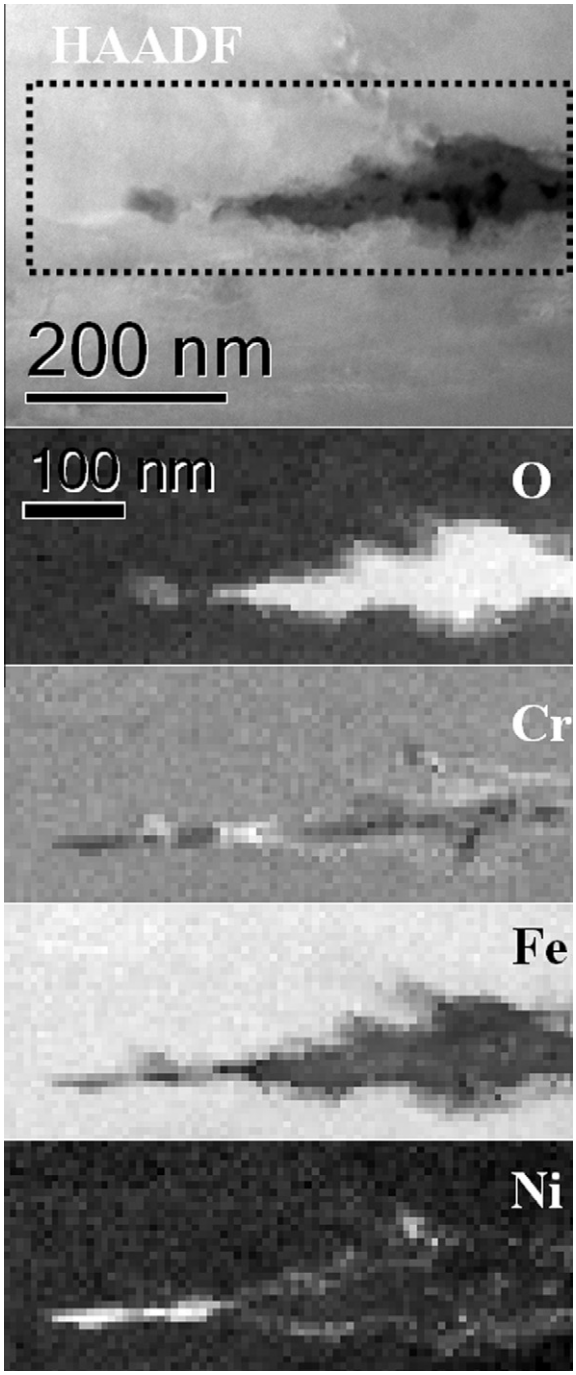

Fig. 7. HAADF image showing detail of dominant crack tip in the SUS304 20%CW sample and EELS elemental maps from boxed region (also displayed in Fig. 6c).

Elastic contrast can be preserved also in HAADF images as a result of channelling along planar or axial directions in crystals. Unless the annular HAADF detector has a large inner acceptance angle (>40 mrad), it will collect a significant proportion of coherent (Bragg) scattering. Even though in our experiments the inner collection semi-angle was >70 mrad, diffraction contrast from defect was observed easily. Grain boundary dislocations may exhibit complicated contrast, going from dark at the entrance surface of the specimen to oscillatory and finally to bright at the exit surface [25]. Similarly, contrast at twin planes in twinned particles of fcc crystals are frequently observed and can be understood with reference to the Ewald sphere [8].

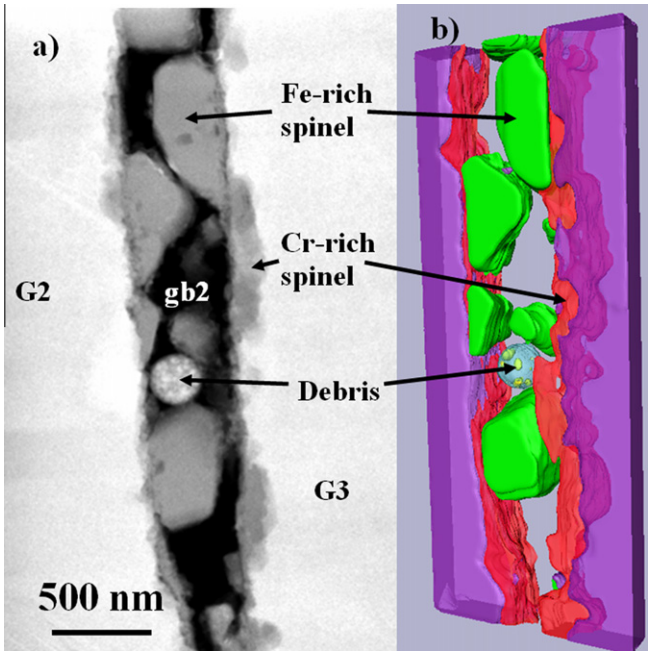

Fig. 8. (a) HAADF image showing a portion of the open crack along grain boundary 2 and ~3 μm from the tip and (b) 3D reconstruction using surface segmentation obtained from an HAADF tomographic series of 69 images (Start tilt: −68.00°; Stop tilt: +72.00°; Tilt step: 2.00°; Exposure time: 15 s) acquired using an inner detector semi-angle of >70 mrad at 300 kV. The particle labelled as "debris" is believed to have entered the open crack through the water. Sample: SUS304 5%CW.

The use of elastic contrast has enabled the accurate measurements of angles between microstructural defects. This information will become very useful when trying to understand the effect of the different defects as stress enhancers under the applied load. Current models have become very close to simulate the crack behaviour in this type of materials [26,27] and would certainly benefit from experimental measurements in 3D. It also proved very useful when characterizing oxidation along TDBs. It a previous work [20] it was noted that initial oxidation only occurred along specific cells inside the TDB, which formed after levels of cold work of 10% or higher. As can be seen in Fig. 9, this is what seemed to have happened. An initially isolated oxide patch inside the TDB can be understood if one assumes that it is connected to the crack flank some distance above the TEM foil plane. Making use of the angular measurements presented in the previous section, it can be calculated that the oxidized cell in the TBD would intersect the crack flank at ~1 μm above the TEM foil or ~1.2 μm along the oxidized cell.

5. Conclusions

A series of novel 3D characterization techniques, applied to the characterization of SCC-related phenomena, have been described in this work. They cover different scales, starting from 3D FIB slicing where volumes as big as 20 × 20 × 20 μm can be reconstructed with high level of detail in a matter of hours. A further step involves the use of electron tomography, which can provide both chemical and crystallographic information on samples which are typically 15 × 10 × 0.1 μm. In order to improve our understanding of the role of cold work in SCC, several samples were characterized using different techniques. 3D FIB slicing has revealed how accelerated oxidation takes place along TDBs which intersect the crack flanks. Electron tomography has been used to visualize the interaction of the microstructure created by the cold work with the crack

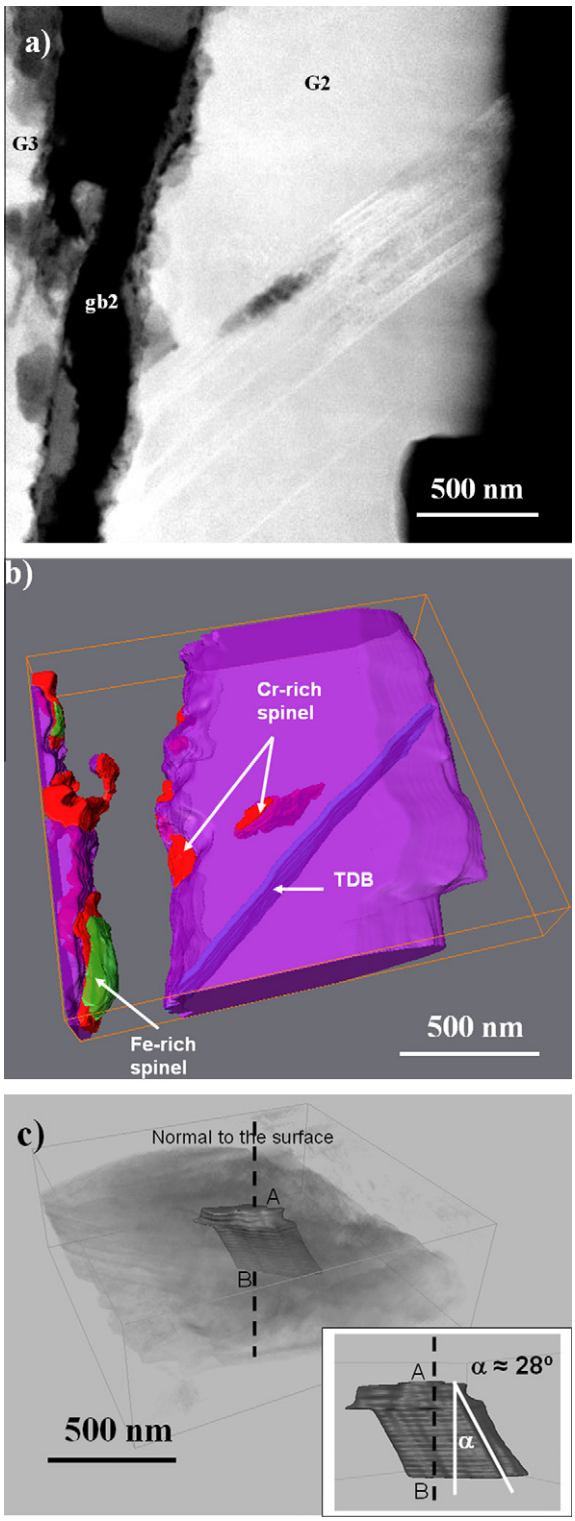

Fig. 9. (a) HAADF image showing a portion of the open crack along grain boundary 2 and ~2.5 μm from the tip. Diffraction contrast from planar defects is visible and (b) visualization of a three-dimensional reconstruction using surface segmentation obtained from an HAADF tomographic series of 69 images (Start tilt: −74.00°; Stop tilt: +74.00°; Tilt step: 2.00°; Exposure time: 15 s) acquired using an inner detector semi-angle of >70 mrad at 300 kV; (c) 3D reconstruction showing the relative orientation of the oxidized TDB in grain 2 respect to the sample surface. Sample: SUS304 5%CW.

tip and has provided with accurate measurements that will be required for future modelling work.

Acknowledgements

Sergio Lozano-Perez is grateful to INSS (Japan) and the Department of Materials (University of Oxford, UK) for sponsoring this research. In particular, Drs. Takumi Terachi and Takuyo Yamada (INSS) are acknowledged for the autoclave testing and useful discussions. The John Fell Fund has fully funded the tomography setup at Oxford. Pilar Rodrigo was supported by the IP3 Project of the 6th Framework Programme of the European Commission: ESTEEM Contract Number 026019.

References

[1] K. Arioka, T. Yamada, T. Terachi, G. Chiba, Corrosion 62 (2006) 568–575.
[2] D.G. Briceno, A.M.L. Hernandez, M.L.C. Marin, Theor. Appl. Fract. Mech. 21 (1994) 59–71.
[3] F. Elfallagh, B.J. Inkson, J. Microsc. 230 (2008) 240–251.
[4] Y. Motoyashiki, A. Bruckner Foit, A. Sugeta, Fatigue Fract. Eng. Mater. Struct. 30 (2007) 556–564.
[5] L. Babout, T.J. Marrow, D. Engelberg, P.J. Withers, Mater. Sci. Technol. 22 (2006) 1068–1075.
[6] L. Robert, N. Brunet, T. Flaherty, T. Randles, E. Matthaei Schulz, H. Vetters, D. Rats, J. von Stebut, Surf. Coat. Technol. 116–119 (1999) 327.
[7] A. King, G. Johnson, D. Engelberg, W. Ludwig, J. Marrow, Science 321 (2008) 382–385.
[8] L.C. Gontard, R.E. Dunin-Borkowski, M.H. Gass, A.L. Bleloch, D. Ozkaya, J. Electron Microsc. 58 (2009) 167–174.
[9] G. Möbus, B.J. Inkson, Appl. Phys. Lett. 79 (2001) 1369–1371.
[10] M.H. Gass, A.E. Porter, Microsc. Microanal. 14 (2008) 668–669.
[11] A. Yurtsever, M. Weyland, D.A. Muller, Appl. Phys. Lett. 89 (2006).
[12] X. Xu, Z. Saghi, R. Gay, G. Möbus, Nanotechnology 18 (2007).
[13] H. Jinnai, T. Kaneko, H. Nishioka, H. Hasegawa, T. Nishi, Chem. Rec. 6 (2006) 267–274.
[14] J.S. Barnard, J. Sharp, J.R. Tong, P.A. Midgley, Science 313 (2006) 319.
[15] M. Eltschka, M. Kläui, U. Rüdiger, T. Kasama, L. Cervera-Gontard, R.E. Dunin-Borkowski, F. Luo, L.J. Heyderman, C. Jia, L. Sun, C. Yan, Appl. Phys. Lett. 92 (2008).
[16] S. Lozano-Perez, Micron 39 (2008) 320–328.
[17] P.A. Midgley, M. Weyland, Ultramicroscopy 96 (2003) 413–431.
[18] J. Gregor, T. Benson, IEEE Trans. Med. Imaging 27 (2008) 918–924.
[19] S. Lozano-Perez, V. de Castro Bernal, R.J. Nicholls, Ultramicroscopy 109 (2009) 1217–1228.
[20] S. Lozano-Perez, T. Yamada, T. Terachi, M. Schröder, C.A. English, G.D.W. Smith, C.R.M. Grovenor, B.L. Eyre, Acta Mater. 57 (2009) 5361–5381.
[21] T. Terachi, T. Yamada, K. Arioka, S. Lozano Perez, in: B. Eyre, I. Kimura, (Eds.), in: Proceedings of the International Symposium on Research for Ageing Management of Light Water Reactors and Its Future Trend, INSS, Fukui, Japan, October 22–23, 2007, pp. 215–228.
[22] B. Schaffer, W. Grogger, G. Kothleitner, Ultramicroscopy 102 (2004) 27–36.
[23] M. Hasimoto, H. Ichinose, Y. Ishida, R. Yamamoto, M. Doyama, Jpn. J. Appl. Phys. 19 (1980) 1045–1050.
[24] D.D. Perovic, C.J. Rossouw, A. Howie, Ultramicroscopy 52 (1993) 353–359.
[25] S. Hillyard, J. Silcox, Ultramicroscopy 58 (1995) 6–17.
[26] A. Stoll, A.J. Wilkinson, Int. J. Fract. (2010) 1–13.
[27] A.P. Jivkov, N.P.C. Stevens, T.J. Marrow, J. Press. Vess. Technol. Trans. ASME 130 (2008) 0314021–0314027.